Validation of X-ray Crystal Structure Ensemble Representations of SARS-CoV-2 Main Protease by Solution NMR Residual Dipolar Couplings

Yang Shen, Angus J. Robertson [†] **and Ad Bax** [*]

Laboratory of Chemical Physics, *National Institute of Diabetes and Digestive and Kidney Diseases, National Institutes of Health, Bethesda, MD 20892, USA*

Correspondence to Ad Bax: bax@nih.gov *(A. Bax)* @angusjrobertson 🐦 *(A.J. Robertson),* @bax_group 🐦 *(A. Bax)*
https://doi.org/10.1016/j.jmb.2023.168067
Edited by M.F. Summers

Abstract

Considerable debate has focused on whether sampling of molecular dynamics trajectories restrained by crystallographic data can be used to develop realistic ensemble models for proteins in their natural, solution state. For the SARS-CoV-2 main protease, M[pro], we evaluated agreement between solution residual dipolar couplings (RDCs) and various recently reported multi-conformer and dynamic-ensemble crystallographic models. Although Phenix-derived ensemble models showed only small improvements in crystallographic R_{free}, substantially improved RDC agreement over fits to a conventionally refined 1.2-Å X-ray structure was observed, in particular for residues with above average disorder in the ensemble. For a set of six lower resolution (1.55–2.19 Å) M[pro] X-ray ensembles, obtained at temperatures ranging from 100 to 310 K, no significant improvement over conventional two-conformer representations was found. At the residue level, large differences in motions were observed among these ensembles, suggesting high uncertainties in the X-ray derived dynamics. Indeed, combining the six ensembles from the temperature series with the two 1.2-Å X-ray ensembles into a single 381-member "super ensemble" averaged these uncertainties and substantially improved agreement with RDCs. However, all ensembles showed excursions that were too large for the most dynamic fraction of residues. Our results suggest that further improvements to X-ray ensemble refinement are feasible, and that RDCs provide a sensitive benchmark in such endeavors. Remarkably, a weighted ensemble of 350 PDB M[pro] X-ray structures provided slightly better cross-validated agreement with RDCs than any individual ensemble refinement, implying that differences in lattice confinement also limit the fit of RDCs to X-ray coordinates.

Introduction

Over 40 years ago, Frauenfelder, Petsko and Tsernoglou noted a significant temperature dependence of the mean-square displacement of atoms in myoglobin crystals and interpreted these in terms of structural dynamics between different sidechain conformations.[1] For proteins that diffract to very high crystallographic resolution, evidence of two sidechain conformations is often observed for multiple residues.[2] Such structural hetero- geneities are considered to be dynamic in nature, and frequently involve discrete sidechain rotamer differences that result in altered backbone geometry, a process known as "backrub motions".[3] At lower resolution, these motions together with other dynamic effects as well as static disorder in the crystalline lattice are accounted for by temperature- or B-factors that are often anisotropic in nature. Such B-factors were qualitatively linked to ^{15}N nuclear spin relaxation rates, measured by solution NMR spectroscopy,[4] that report on the

amplitudes and time scales of orientational fluctuations of backbone amide N—H bond vectors. Joint analysis of NMR relaxation rates and anisotropic displacement factors of high-resolution X-ray data can further extend such analyses, providing detailed insights into both the time scales and amplitudes of internal motions.[5]

Over the past few decades, multiple new methods have been introduced to interpret B-factors and their anisotropies in terms of ensemble representations of conformers, potentially providing atomic level insights into the dynamic features of proteins that are essential to their function. In particular, the powerful Phenix software[6,7] has become widely used for this purpose. For structures of sufficient crystallographic resolution, in practice typically better than *ca* 1.6-Å, the use of multiple (but usually just two) conformers to represent the structure can yield improved fits to the observed electron density.[2] In such multi-conformer representations, each conformer and its fractional population are reasonably well defined. On the other end of the spectrum, ensemble representations have been generated to represent dynamic X-ray structures, where a large number of conformers are used to fit the electron density with the aim of yielding a representative ensemble, while lacking the uniqueness of the multi-conformer representation in the selection of individual ensemble members.

The X-ray ensemble representation appears superficially similar to the bundle-of-structures representation commonly used for protein atomic coordinates derived from NMR data, but there are pivotal differences: The NMR bundle width is strongly and inversely correlated with the number and precision of local restraints, with more measurements typically giving rise to a sharper definition of the structure, or a narrower bundle width. The bundle width therefore usually does not represent true dynamics but is dominated by the limited restraint power of the input data. By contrast, the X-ray ensembles aim to represent the minimum amount of conformational heterogeneity needed to adequately explain the observed X-ray diffraction data. In this case, an increased bundle width indicates that the X-ray data cannot be fitted by a single set of atomic coordinates and positively identifies dynamics. However, the question to what extent the ensemble reflects rapid dynamic fluctuations versus small heterogeneities in the crystal can be difficult to answer.

An early method for representing X-ray crystal structures as realistic ensembles of low energy structures, without introducing human bias, sampled molecular dynamics (MD) trajectories that were recorded while imposing time-averaged crystallographic restraints.[8] This development followed the use of distance-restrained MD trajectories for representing structures that satisfy the time-averaged, $(r^3)^{-1/3}$-weighted NOE distances measured by solution NMR.[9] However, even while such MD-derived X-ray structure ensembles provided much improved fits to the X-ray structure factors, cross-validation analyses based on the crystallographic free R factor (R_{free})[10] pointed to significant over-fitting of the data.[11,12] Subsequently, multiple improvements to MD-based ensemble modeling of X-ray structures have been introduced and incorporated in the Phenix software suite for defining macromolecular structures based on crystallographic data. Starting from a refined X-ray structure, Burnley et al. developed a modified procedure to generate an ensemble of conformers from a molecular dynamics trajectory with time-averaged restraints to the crystallographic electron density.[13] This procedure eliminated the over-fitting by limiting the number of structures used to fit the electron density while separating the effects of global disorder, possibly resulting from lattice distortions, from true dynamic effects. Using anywhere from 39 to 600 ensemble members, improvements in R_{free} of, on average, nearly 2% (*i.e.* by *ca* 10% of their actual values of ~20%) were obtained for a set of 20 X-ray structures, spanning a range from 1.1 to 3.1-Å in crystallographic resolution.[13]

More recent enhancements in X-ray ensemble generation use the elastic net approach [14] to regularize the underdefined ensemble by allowing disorder only for a smaller unit of structure when the data cannot be fitted to disorder on a larger scale.[15] The elastic net has been implemented in Phenix as deformable elastic network (DEN) restraints.[16] Heterogeneity at each level is described by torsion-libration-screw (TLS) transformations, which provide a convenient method for parameterizing rigid body displacements and provide insights into the mechanics of the internal motions.[17,18] In their pTLS implementation of ensemble refinement, Burnley et al. used an iterative procedure to define the protein atoms with large B-factors while using only the remaining percentage, 'p', to define the pTLS parameters for global disorder of the protein within the lattice.[13] However, the pTLS analysis can result in an overly tightly defined ensemble for the well-ordered regions of a protein. This problem has been addressed in the newly introduced ECHT refinement, where disorder is broken down to different size scales; that of the intact chain, of elements of secondary structure, or at the residue level.[15] Importantly, if disorder at different levels is uncorrelated, the overall dynamics can be described as the sum of the motions at each ECHT level. We note that all these ensembles typically only use Bragg reflections as experimental restraints and ignore the diffuse scattering intensity that contains experimental information on the collectiveness of internal motions,[19] and therefore solely derive the information on collectiveness of motion from the restrained MD calculations.

Recently, Ploscariu *et al.* applied the ECHT ensemble refinement, including DEN restraints, to three small proteins and to the SARS-CoV-2 main protease homodimer, the latter starting from X-ray data that originally had been used do derive a 1.2-Å resolution multi-conformer model (PDB entry 7K3T).[20] They first re-refined the 7K3T structure using *PDB-REDO*,[21] prior to using it as input for their ensemble refinements. Results were compared to those obtained with the earlier pTLS method that lacked DEN restraints,[13] with ECHT refinement yielding small further improvements in R_{free} for some, but not all, of the proteins tested, while providing physically interpretable models for the types of motions that contributed to the observed disorder. Ensembles each consisting of 50 members for both pTLS and for three ECHT levels were presented and deposited by Ploscariu et al.,[20] where ECHT level 1 corresponds to global protein disorder (chain level), ECHT level 2 additionally includes disorder at the secondary structure level, and level 3 also includes the residue level, with all refinements carried out using DEN restraints during the MD simulations.

Residual dipolar couplings (RDCs), measured by solution NMR spectroscopy for proteins that are very weakly aligned relative to the external magnetic field, are highly precise reporters on the orientation of internuclear vectors.[22,23] Measured RDCs correspond to their time-weighted average over a very broad range of time scales, spanning from sub picoseconds to milliseconds. As a consequence, vectors that sample a wide range of orientations generally will yield smaller RDCs than expected for their static, time-averaged orientation.[24,25] We recently reported a nearly complete set of one-bond ^{15}N-$^{1}H^{N}$ RDCs ($^{1}D_{NH}$) for the SARS-CoV-2 main protease, as well as a complementary set of two-bond $^{13}C'$—H^{N} ($^{2}D_{C'H}$) RDCs involving the carbonyl carbon, and we compared their agreement with 350 X-ray structures available in the PDB.[26] With quality factors, Q,[22] as low as 0.21 these RDCs agreed well for the most ordered regions of both the high-resolution X-ray structures as well as AlphaFold2 models, but showed considerably lower agreement ($Q \approx 0.35$) for both its center domain and its C-terminal α-helix, suggesting that dynamics strongly impacted the RDCs.[27,28] Agreement between solution RDCs and X-ray structures is also quite sensitive to the quality of X-ray structures, with Q factors below 0.2 generally only attainable for X-ray structures solved at better than 2-Å resolution,[29] and Q factors sometimes approaching 0.1 for smaller proteins or when averaging vector orientations obtained from independently determined X-ray structures.[30]

Here, we evaluate the agreement between RDCs measured for a stable active site mutant of M^{pro}, C145A,[26] and both multi-conformer and pTLS-ensemble representations of X-ray structures, previously reported for the native apo-enzyme at temperatures ranging from 100 to 310 K.[31] We also test agreement with the recently reported ECHT-1 ensemble[32] which is found to yield an improved fit to RDC data for the more disordered regions of the protein.

Results and discussion

In the principal axis frame of the molecular alignment tensor, the RDC between two atomic nuclei, *A* and *B*, is given by

$$D^{AB}(\theta, \phi) = D_a^{AB}\left[(3\cos^2\theta - 1) + \frac{3}{2}Rh\sin^2\theta\cos(2\phi)\right] \quad (1)$$

where θ and φ are the polar coordinates of the *A-B* vector. The orientation of the alignment tensor relative to the molecular frame is defined by three Euler angles. These three angular parameters together with the strength of the alignment, D_a^{AB}, and its rhombicity, Rh, are optimized when using singular value decomposition (SVD) to find best agreement between experimental RDCs and the corresponding vector orientations.[33] The SVD is carried out in the molecular frame, but the extracted symmetric and traceless 3 × 3 Saupe matrix can be transformed to the principal axes system (PAS) alignment frame where the tensor becomes diagonal, resulting in the simple form of Eq. (1). In Eq. (1), D_a^{AB}, corresponds to half the maximum possible value for an RDC, which applies for an *A-B* vector that is aligned along the *z*-axis of the PAS. Besides the strength of molecular alignment, D_a^{AB} scales with the inverse cube of the internuclear distance, r_{AB}^3, and with the product of the magnetogyric ratios, γ_A and γ_B. However, when considering a specific type of internuclear vector, such as that of backbone amide ^{15}N-^{1}H pair, the internuclear distance can be treated as uniform across the entire protein, resulting in a single D_a^{NH} interaction constant. Its size, as well as the rhombicity of the alignment tensor, Rh, and the 3 angles that define the PAS follow directly from the SVD fit.[34]

Natively, the M^{pro} enzyme is a 68-kDa (2 × 306 residue) homodimeric protein complex with C_2 symmetry on the NMR time scale. So, even while on a time scale of microseconds or shorter, small asymmetries will be present in the dimer, these average out on the millisecond time scale of NMR observation. The dimeric protein therefore gives rise to a single set of resonances. Moreover, for a C_2-symmetric homodimer, one of the principal axes of the alignment tensor coincides with the C_2-symmetry axis,[23] effectively reducing the number of independent variables from five to three when best fitting the RDCs to the molecular coordinates. Because the orientation of the alignment tensor cannot be restrained when using the SVD algorithm, a simple and effective workaround is used, where the number of observed RDCs is artificially doubled by assigning the same experimental RDC to pairs of corresponding vectors of the homodimer and applying the SVD to the homodimer rather than to the monomer.

For the two-bond $^{13}C'-^1H^N$ internuclear vector, a small degree of variation in the $^{13}C'-^1H^N$ distance will occur with variations in the $C'-N-H$ covalent bond angle, but such variations are ignored during the SVD fit. In principle, the relative strength of the alignments, D_a^{NH} and $D_a^{C'H}$, is known from the peptide bond geometry. However, because $^1D_{NH}$ and $^2D_{C'H}$ values were measured several weeks apart, and sample alignment slowly decreased with time due to finite stability of the alignment medium used (filamentous *Pf1* phage[35]), their alignment parameters were determined independently.

Sensitivity of RDCs to procedure used for adding H atoms

The fits of experimental RDCs to protein X-ray structures are quite sensitive to the method used for adding hydrogens to the X-ray structures. Typically, when included as part of deposited X-ray structures, the H-atom coordinates are in poor agreement with RDC data and therefore the hydrogens are first stripped off the coordinate set, and subsequently added by modeling software. None of the programs used for this purpose is perfect because the H-atom position is sensitive to remote steric effects from sidechains and hydrogen bonding that are not easily accounted for.[36] In practice, we find that addition of hydrogens by XPLOR-NIH,[37] MOLMOL,[38] ROSETTA,[39] or the Dynamo module of NMRPipe[40] yields fits to the $^1D_{NH}$ RDCs that are of comparable quality, but considerably better than, for example, obtained with REDUCE,[41] which uses a nearly 5° smaller in-plane H-N-Cα angle of 114° than the other programs (Table 1). The programs also differ with respect to the definition of the peptide plane in which the hydrogen is located (Table 1), but the resulting differences in N—H vector orientation are smaller and have less impact on the quality of RDC fits. The different but uniform N—H bond length used by the various programs (Table 1) do not impact the quality of the $^1D_{NH}$ fit because it simply scales the D_a^{NH} value of Eq. (1). However, the N—H bond length has a noticeable effect on the in-plane $C'-H^N$ vector orientation which changes

orientation by *ca* 1.5° when the N—H bond length is reduced from 1.04 to 0.99 Å. The 1.04-Å bond length is sometimes used to account for a decrease in the $^1D_{NH}$ coupling relative to $^1D_{CC}$ and $^1D_{NC}$ couplings, caused by the substantial amplitude of normal-mode librations of the N—H bond.[42] However, for evaluation of $^2D_{C'H}$ couplings, best agreement is obtained when using a 0.99-Å bond length[26] and this value is used here in all our analyses of $^2D_{C'H}$ couplings.

Sensitivity of RDCs to vector orientation

Even though the overall fit of experimental RDCs to molecular coordinates is valuable for evaluating the accuracy of structural models,[43,44] it is important to note that the change in an RDC for a given small change in its internuclear orientation greatly varies for different vectors.[22] For example, for any internuclear vector that is parallel to any of the three principal axes of the alignment tensor, the derivative of its RDC with respect to orientation is zero. The derivative of $D^{AB}(\theta,\phi)$ with respect to its polar coordinates is given by

$$\frac{d[D^{AB}(\theta,\phi)]}{d\theta} = D_a^{AB}\left[-3\sin(2\theta) + \frac{3}{2}Rh\ \sin(2\theta)\ \cos(2\phi)\right]$$
(2a)

$$\frac{d[D^{AB}(\theta,\phi)]}{d\phi} = -D_a^{AB}[3\ Rh\ \sin^2\theta\ \sin(2\phi)]$$
(2b)

which results in a sensitivity to vector orientation, Ω, given by

$$\frac{d[D^{AB}(\theta,\phi)]}{d\Omega}$$
$$= D_a^{AB}\sqrt{\left\{[-3\sin(2\theta) + 3/2Rh\ \sin(2\theta)\ \cos(2\phi)]^2 + [3\ Rh\ \sin\theta\ \sin(2\phi)]^2\right\}/2}$$
(2c)

Figure 1 visualizes this sensitivity of RDC to vector orientation for M^{pro}, using the alignment tensor obtained from the RDC fit of all previously reported $^1D_{NH}$ and $^2D_{C'H}$ values[26] to the coordinates of the 1.2-Å X-ray structure in its homodimeric, apo state. The same color coding used for highlighting this differential RDC sensitivity to vector orientation is mapped onto the backbone of the 7K3T X-ray structure, with chain A depicting the derivative (Eq. (2c)) for N—H vectors and chain B for $C'-H^N$ vectors.

Accuracy of RDC measurements

A lower-bound estimate of the uncertainty in $^1D_{NH}$ RDC measurements can be obtained from the signal to noise ratio in the ARTSY spectra used to measure their values,[45] and from the line width and signal to noise in the TATER-HNCO spectra for the $^2D_{C'H}$ values.[26] However, these estimates neglect the presence of potential systematic errors such as imperfect phasing or baseline distortions. Here, we show that a good estimate of the true

Table 1 Orientation of N—H bond vectors as defined by various software packages.

	Plane	In-plane orientation	Bond length (Å)
Dynamo[a]	C_{i-1}^α-C'_{i-1}-N_i	bisector	1.02
Xplor[a]	C_{i-1}^α-C'_{i-1}-N_i	bisector	0.98
Molmol	C'_{i-1}-N_i-C_i^α	H_i-N_i-C_i^α = 118.0°	1.01
Rosetta	C'_{i-1}-N_i-C_i^α	H_i-N_i-C_i^α = 119.2°	1.01
Reduce	C'_{i-1}-N_i-C_i^α	H_i-N_i-C_i^α = 114.0°	1.00

[a] Minor adjustments to the listed values are made by these programs to reduce steric clashes.
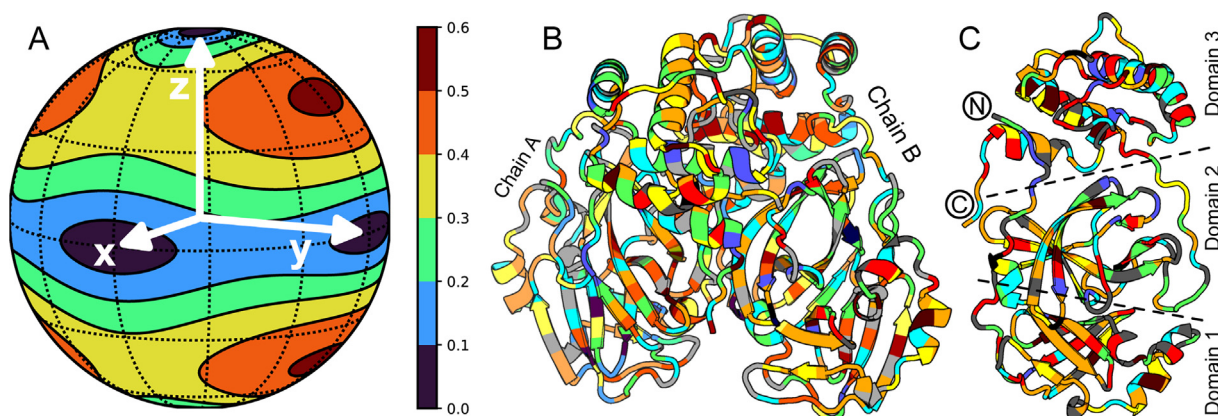
Figure 1. Sensitivity of RDCs to structural noise. (A) Color map of the sensitivity of $^1D_{NH}$ to the N—H vector orientation in the principal axis system (white) of the M^{pro} alignment tensor. Values correspond to a 1° random change in orientation. (B) Ribbon diagram of the 7K3T M^{pro} homodimer X-ray structure. Colors correspond to the sensitivity of RDCs to orientation for the $^1D_{NH}$ values (chain A) and for the $^2D_{C'H}$ couplings, mapped on chain B; residues lacking a measured RDC are in grey. (C) Ribbon diagram for the monomeric subunit, with labeling of the N- and C-terminal residues and marking of the N-terminal domain (domain 1), the central domain (domain 2), and the α-helical C-terminal domain (domain 3) that is key to dimerization. The active site is at the interface between domains 1 and 2.

uncertainty in the experimental RDCs can be obtained by evaluating their agreement with the X-ray structure for vectors that are only weakly dependent on orientation (*cf* Eq. (2c)). In this evaluation we also exclude vectors for which the width of the angular distribution in the X-ray ensembles falls in the top 30%, because the precision at which the coordinates are known is lower for these dynamic residues.

After discarding RDCs for vectors that fall in this top 30% of dynamic residues when considering all 381 chains of eight X-ray ensembles (Table 2), with angular rmsd cut-off values of 11.5° for NH, and 11.8° for C'H, the remaining RDCs (178 $^1D_{NH}$ and 179 $^2D_{C'H}$) were grouped according to their sensitivity to orientation. The root-mean-square difference (RMSD) between observed RDCs and values predicted by the structure will be dominated by NMR measurement error for vectors whose RDCs are least sensitive to orientation. Conversely, the quality of the fit will become dominated by coordinate uncertainties for vectors most sensitive to orientation. A plot of the RMSD between observed and predicted values shows a nearly linear increase with their sensitivity to orientation (Figure 2), with a Y axis intersect of *ca* 1.2 Hz for $^1D_{NH}$ but somewhat higher (∼2 Hz) for the $^2D_{C'H}$ couplings after they were upscaled by a factor of 3.09 to normalize them relative to the $^1D_{NH}$ values.

The above derived experimental RDC errors are larger than prior estimates of *ca* 0.5 Hz for both $^1D_{NH}$ and $^2D_{C'H}$ (prior to upscaling by 3.09) that were based solely on signal-to-noise and line width and ignored effects from baseline imperfections and line shape distortions.[26] However, for both types of RDCs the experimental

errors remain substantially below the RMSD between observed and best-fitted values when considering the full sets of RDCs. The reported Q factors are therefore dominated by coordinate uncertainties, with only little impact from the RDC measurement errors.

Agreement of RDCs with 7K3T ensembles

Using newly introduced procedures, Ploscariu *et al.*[32] derived multiple ensemble representations for the 1.2-Å X-ray structure of M^{pro}, with the original data collected at 100 K.[20] Out of 350 sets of M^{pro} coordinates available in the PDB, including both apo and ligated structures, this 7K3T structure[20] is among the top 1% in terms of agreement with RDCs.[26] Nevertheless, with a jackknifed quality factor, Q_{jk} (see Methods) of 0.265, this agreement is lower than expected for a protein structure that is well refined at such a high level of resolution.[29,46] A small improvement in this fit, most noticeable for the $^2D_{C'H}$ couplings, was observed when using as input for the SVD fit the coordinates obtained by Ploscariu after re-refinement with *PDB-REDO*[21] (Table 2). For both the original 7K3T and its *PDB-REDO* coordinates, about two dozen residues adopt two different conformations, with different weights. In our SVD fits of the RDCs to these structures, we use a 100-member ensemble coordinate representation of these multi-conformer datasets, where each discrete conformer is represented Z times when Z is the percentage occupancy listed in the PDB entry. For all such datasets, this method for SVD fitting of the RDCs resulted in a small Q_{jk} decrease, by as much as 0.01 for the *PDB-REDO* 7K3T coordinates, over simply fitting the conformer with the highest occupancy (SI Table S1).

Table 2 Agreement between RDCs and X-ray structures of M[pro], recorded at different temperatures, and refined as standard multi-conformer or ensemble representations.[a]

Structure	X-ray					NMR			
	T (K)	Resolution (Å)	R_{free}	N[b]	DEN restraints	$^1D_{NH}$ & $^2D_{C'H}$		$^1D_{NH}$	$^2D_{C'H}$
						$<D_a>$	$<Rh>$	Q_{jk}	Q_{jk}
7K3T	100	1.2	0.187	2	NA	12.727	0.356	0.265	0.265
7K3T-REDO[c]	100	1.2	0.173	2	NA	12.735	0.356	0.265	0.254
pTLS[c]	100	1.2	0.169	50	Yes	13.261	0.357	0.238	0.232
ECHT-1[c]	100	1.2	0.176	50	Yes	13.679	0.357	0.233	0.230
7MHF[d]	100	1.55	0.224	2	NA	12.641	0.377	0.266	0.253
7MHL	100	1.55	0.227	54	No	13.385	0.373	0.288	0.264
7MHG[d]	240	1.53	0.205	2	NA	12.623	0.384	0.247	0.236
7MHM	240	1.53	0.197	43	No	13.298	0.381	0.252	0.234
7MHH[d]	277	2.19	0.253	2	NA	12.515	0.378	0.299	0.287
7MHN	277	2.19	0.215	45	No	13.602	0.381	0.293	0.265
7MHI[d]	298	1.88	0.228	2	NA	12.521	0.384	0.240	0.247
7MHO	298	1.88	0.208	75	No	13.658	0.376	0.280	0.268
7MHJ[d]	298[e]	2.0	0.240	2	NA	12.514	0.381	0.270	0.283
7MHP	298[e]	2.0	0.221	28	No	13.775	0.380	0.269	0.240
7MHK[d]	310	1.96	0.247	2	NA	12.512	0.381	0.245	0.286
7MHQ	310	1.96	0.235	36	No	13.746	0.378	0.269	0.267
AF2-1[f]				1	NA	12.597	0.354	0.239	0.236
AF2-*[g]				25	NA	12.641	0.354	0.239	0.235
7K3T+[h]	100	1.2		100	Yes	13.164	0.352	0.230	0.229
7MH*[i]	100–310	1.53–2.19		281	No	13.815	0.372	0.230	0.216
MproEE[j]	100–310	1.2–2.19		381	Partial	13.881	0.378	0.214	0.207
Xray*[k]	Various	1.2–2.85		350	NA	13.092	0.358	0.218	0.208
Xray*-VWfit[l]	Various	1.2–2.85		350	NA	12.966	0.366	0.210	0.203

[a] X-ray structures from reference 31, RDCs from reference 26, with the $^2D_{C'H}$ upscaled by a factor 3.09 to account for differences in applicable magnetogyric ratios, internuclear distances, and slightly different alignment strength for the $^2D_{C'H}$ and $^1D_{NH}$ measurements. RDCs for very strongly disordered C-terminal residues V303 to Q306 were excluded from the RDC analysis.

[b] N is the number of conformers.

[c] Coordinates of 7K3T-REDO, and pTLS and ECHT-1 ensembles of the 7K3T dataset are taken from the supplemental Zenodo repository of 32.

[d] Fitting results for the corresponding structures recalculated by PDB-REDO are shown in Table S4.

[e] At 99.5% relative humidity.

[f] Top AlphaFold2-multimer model.

[g] Unweighted ensemble of top 25 AlphaFold2-multimer models.

[h] Unweighted combined 7K3T pTLS and ECHT-1 ensembles.

[i] Unweighted combination of six ensembles of 7MHL-7MHQ, recorded at temperatures ranging from 100 to 308 K.

[j] Unweighted combination of eight ensembles: 7K3T pTLS and ECHT-1, together with 7MHL-7MHQ.

[k] Equally weighted ensemble of 350 PDB X-ray structures.

[l] Ensemble of 350 PDB X-ray structures with weights optimized by VWfit[30] reported in column 2 of Table S2.

A substantial further improvement for the fits of both the $^1D_{NH}$ and $^2D_{C'H}$ couplings to the coordinates was obtained for the DEN-restrained pTLS ensemble representation of 7K3T, with Q_{jk} values improving from 0.265 to 0.238 (Table 2).

Assuming that the ensemble vector orientations correspond to rapid (<1 ms) dynamic excursions relative to their averaged orientation, these motions decrease the RDC by a generalized order parameter, S, relative to that for a static vector at the averaged orientation.[47] For N—H angular excursion of amplitude β_n in ensemble member n relative to its ensemble-averaged orientation, S is given by

$$S = \{3\langle cos^2 \beta_n \rangle - 1\}/2 \qquad (3)$$

where the averaging extends over the 50 members of the 7K3T pTLS ensemble. The angular excursions of N—H

and C′—H vectors, $\beta_{n,NH}$ and $\beta_{n,C'H}$, are strongly correlated (Figure S1(A)) because they are dominated by so-called crankshaft or γ motions around the C^α_{i-1}–C^α_i axis.[5,48,49] Both N—H and C′—H vectors are nearly orthogonal to this axis. Thus, the RMS amplitudes, $\sqrt{<\beta^2_{n,NH}>}$ and $\sqrt{<\beta^2_{n,C'H}>}$, are also strongly correlated (Figure S1(B)) and we therefore use their pairwise-averaged value

$$\beta_{n,A} = \sqrt{\left(\langle \beta^2_{n,NH} \rangle + \langle \beta^2_{n,C'H} \rangle \right)/2} \qquad (4)$$

as a measure for the amplitude of local angular excursion at peptide plane n. In the 7K3T pTLS ensemble, these values span a wide range from as low as 1.6° for α-helix I200-I213 to >33° for C-terminal residues S301-Q306 (Figure S2(A)).
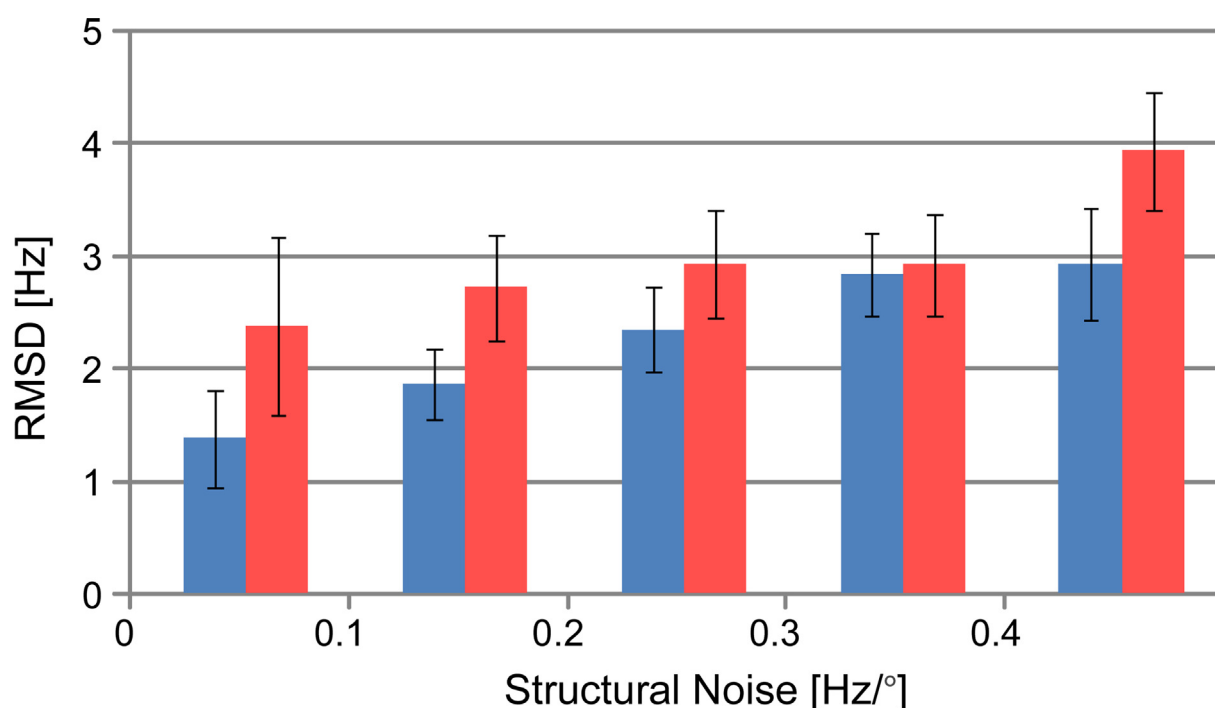
Figure 2. RMSD between observed and predicted $^1D_{NH}$ (blue) and $^2D_{C'H}$ (red) RDC values, for vectors with binned sensitivity to internuclear vector orientation ranging from ≤0.1 Hz/° to >0.4 Hz/°, as derived from Eq. (2c). Only the 70% of N—H and C'—H vectors with lowest angular distributions in the 381-member super ensemble of X-ray structures (Table 2) were used for this analysis. The RMSD is calculated from a global SVD fit of all RDCs to the *PDB-REDO* coordinates of the 7K3T structure, with protons added by Dynamo. Experimental $^2D_{C'H}$ values were upscaled by a factor 3.09 to normalize them relative to $^1D_{NH}$.

A histogram of the root-mean-square distribution of $\beta_{n,A}$ values for the pTLS ensemble shows that for about half of the residues $\sqrt{<\beta_n^2>}$ is smaller than 6°, but with significant tailing to larger amplitudes (Figure 3). Replotting these values as generalized order parameters (Eq. (3)) highlights the locations of the most dynamic regions in the corresponding ensembles (Figure 4) and appears qualitatively similar to the M^{pro} B-factor profile shown by Pearce and Gros[15] and the C^α RMSD plot of Ploscariu *et al.*[32]

The ECHT disorder models for M^{pro} deposited by Ploscariu *et al.* aim to select physically plausible global and local disorder on which the DEN- and X-ray-restrained MD-derived motions are superimposed. The ECHT-1 chain level of disorder is pertinent to our NMR analysis because it includes all internal protein motions at any scale level, but not the disorder of individual chains in the crystal lattice that does not affect RDCs. The higher levels of ECHT analysis are valuable for providing insight into the types of internal motions present, but RDCs can only provide information at this level of detail when they are measured under multiple, linearly independent alignment conditions,[50,51] or if a large number of different types of RDCs can be measured at very high preci-

sion,[52] which is not the case for M^{pro}. ECHT-2 and ECHT-3 M^{pro} ensembles are therefore not included in our analysis.

Ensembles refined at the ECHT-1 level show relatively large heterogeneity in the amplitude of excursions during the restrained MD trajectory after heterogeneity at the chain level has been factored out. Even though the R_{free} is slightly higher for the ECHT-1 than the pTLS ensemble, a very small improvement in RDC fits of ECHT-1 over the pTLS ensemble is observed, with each being 10–15% better than obtained for a fit to the *PDB-REDO* 7K3T coordinates (Table 2). Remarkably, when fitting the pTLS and ECHT-1 jointly as a single 100-member ensemble, the Q_{jk} values improve further, by a few percent, suggesting that the distribution of $\sqrt{<\beta_{n,A}^2>}$ values in each of these ensembles contains outliers for different residues, which become attenuated after considering the ensembles jointly (Figure S2). Indeed, plotting the $\sqrt{<\beta_{n,A}^2>}$ values of the pTLS ensemble against those of ECHT-1 shows considerable scatter, more than what is observed when comparing the dispersion in C^α coordinates (Figure 5).

For a given alignment tensor, high X-ray ensemble disorder lowers the predicted RDCs.
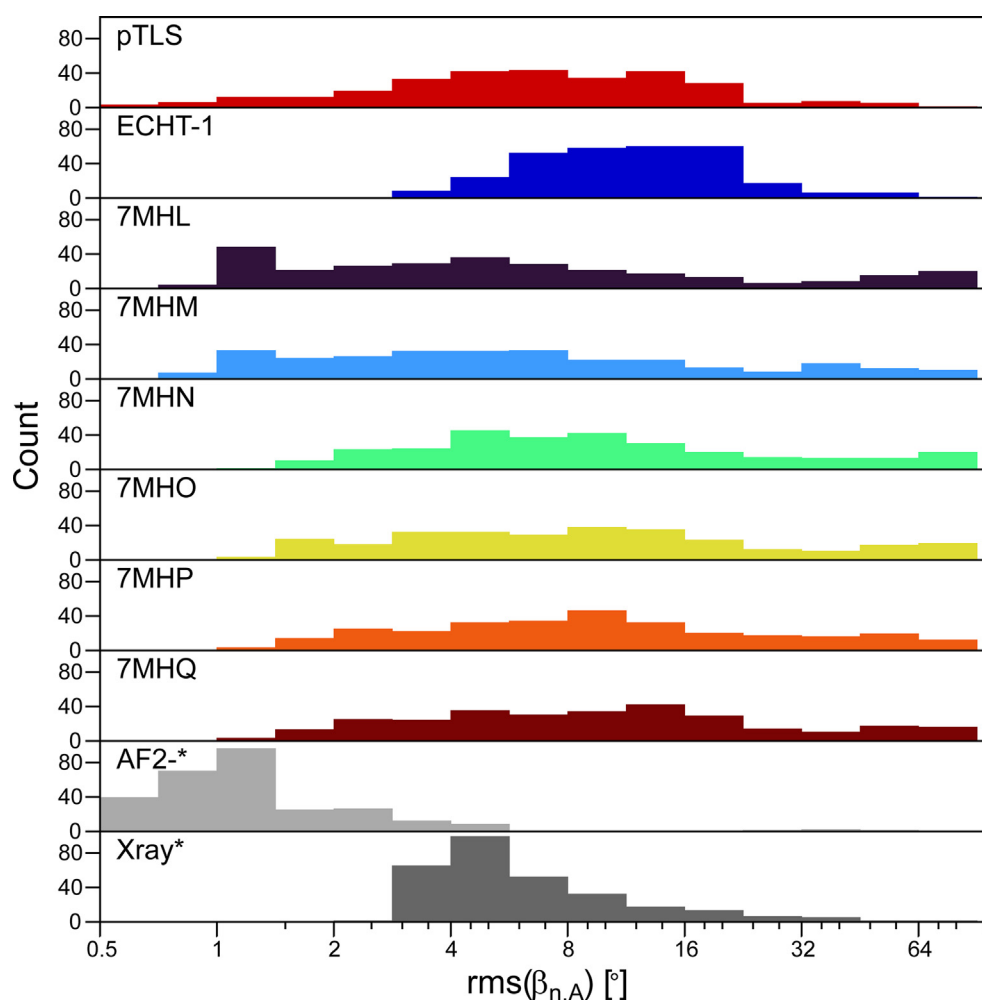
Figure 3. Distribution of the rms angular variations, $\sqrt{<\beta_{n,A}^2>}$ of backbone amide orientations in various ensemble representations of M^{pro}. The distributions are for 254 M^{pro} residues for which N—H and/or C'—H RDCs were previously measured. See Table 2 for temperatures at which each structure was recorded. AF2-* represents an ensemble of 25 AlphaFold-2 models (see Methods). The Xray* ensemble consists of 350 X-ray depositions that had no missing residues (Table S2).

Thus, if true disorder is less than presented in the X-ray ensemble, fitting the alignment tensor to experimental RDCs will increase the fitted alignment strength, D_a, to bring predicted and observed RDC values in agreement. Comparison of the alignment strength, D_a, when fitting the coordinates of the pTLS and ECHT-1 ensembles shows a nearly 4% higher value for the latter, reflecting the larger values of $\sqrt{<\beta_{n,A}^2>}$ in the ECHT-1 ensemble (Figure S2).

RDC evaluation of ensemble representations for dynamic and static regions

The ECHT-1 M^{pro} ensemble representation shows substantial variation in backbone disorder. It therefore is of interest to evaluate whether the improvements in RDC fits observed for ensemble over conventional representations are dominated by better fits for the ostensibly more flexible residues, or whether the improved fit applies similarly across the entire chain. For this purpose, we arbitrarily separate the M^{pro} residues in two equally sized groups according to the rms amplitude of the angular excursions of the N-H and C'-H vectors in the ensembles, $\sqrt{<\beta_{n,A}^2>}$, and refer to these as low (L50%) and high (H50%) dynamic groups.

We found that for both the pTLS and ECHT-1 ensembles the fit to the RDC data is considerably better for the L50% group of residues than for H50% (Table 3). This difference becomes even more pronounced when considering the conventional 7K3T representations of M^{pro}, consistent with the expectation that the low agreement between RDCs and such a static representation is strongly impacted by dynamic effects.
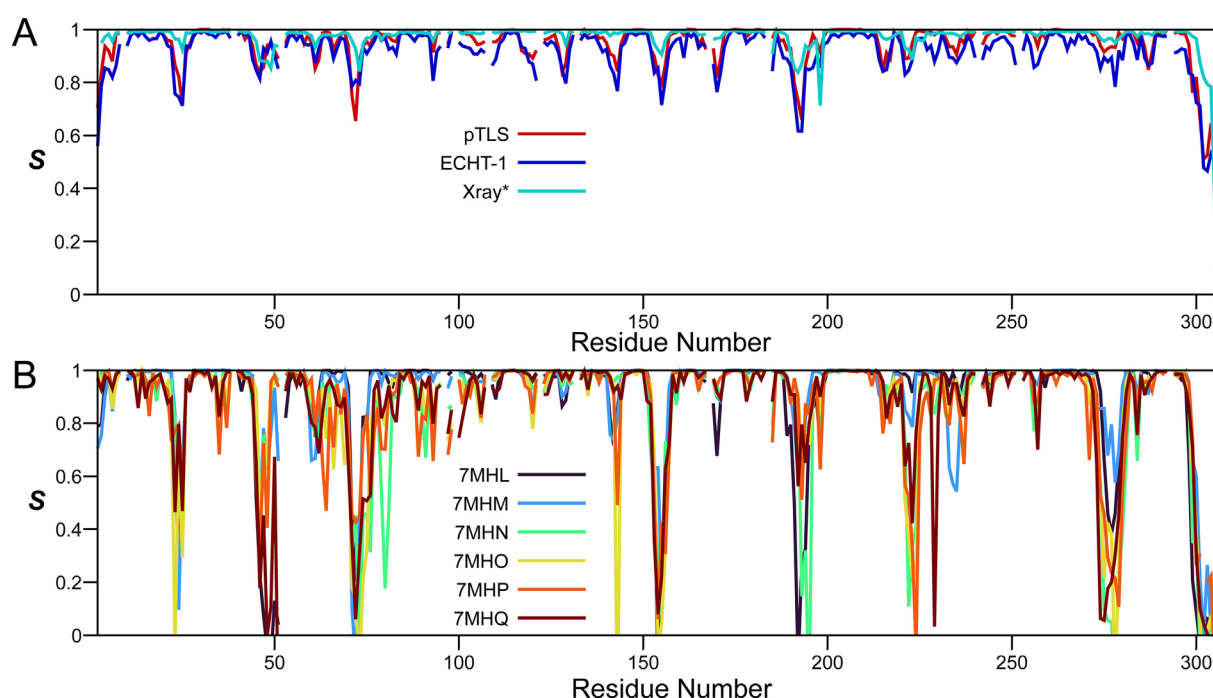
Figure 4. Generalized backbone order parameter, **S**, as a function of residue number in different ensemble representations of M^{pro}, obtained from Eq. (3). (A) Ensembles obtained for 7K3T PDB-REDO using pTLS (red) and ECHT-1 (blue) methods, with the **S** values corresponding to an ensemble comprising all 350 PDB X-ray structures shown in turquoise. (B) Ensembles reported by Ebrahim et al.[31] for M^{pro} X-ray structures at different temperatures (see Table 2). Correlation graphs between the various order parameters are shown in Figure S7.

For L50%, we found that pTLS and ECHT-1 ensemble representations lower the Q_{jk} factor *ca* 8 and 5%, respectively, over the conventional *PDB-REDO* 7K3T structure. For the most dynamic half of residues, the corresponding Q_{jk} improvements were *ca* 16 and 20%, with the larger improvement observed for the ECHT-1 ensemble. This result suggests that ECHT-1 better represents the dynamic residues than the pTLS ensemble, with the opposite applying for the least dynamic half. However, the difference in D_a values obtained when separately fitting L50% and H50% residues (Table 3) indicates that the amplitude of motions in H50% is too large (*vide infra*).

As discussed below, we do not observe similar levels of improved agreement when comparing conventional with their corresponding ensemble representations for the temperature series of X-ray structures of Ebrahim *et al.*[31] (Table 3), although substantial improvements are obtained when merging all their ensemble members into a single "super-ensemble".

Agreement of RDCs with X-ray ensembles recorded at different temperatures

We also evaluated agreement between the $^1D_{NH}$ and $^2D_{C'H}$ RDCs, recorded in solution at 298 K, and the M^{pro} X-ray ensembles obtained at temperatures ranging from 100 to 310 K, as well as their corresponding conventional multi-conformer structures.[31] Importantly, in contrast to the above discussed ensembles derived from the 7K3T X-ray structure, the ensemble refinements used for this temperature series of X-ray structures did not include the newly introduced innovations of DEN restraints during the MD trajectory and also used a much larger fraction of residues (80% *vs* 30%) to define the baseline for the pTLS analysis. The resulting ensembles showed excellent R_{free} statistics[31] but considerably larger differences between R_{work} and R_{free} than in the Ploscariu study.[32]

While their crystallographic resolution was highest at low temperatures (100 and 240 K), which normally would be expected to result in better fits to RDCs,[29,46] best agreement between the most precisely measured $^1D_{NH}$ RDCs (*c.f.* Figure 2) and any of the conventional representations was obtained for the 298-K 1.88-Å X-ray structure (PDB entry 7MHI; Table 2). The observation that best agreement with RDCs is obtained at room temperature, despite the somewhat lower crystallographic resolution, suggests that small true shifts in the M^{pro} structural distribution at 100 and 240 K approximately offset the effects of higher crystallographic resolution at these lower temperatures. This result is consistent with earlier findings that conformational distributions can shift with tempera-
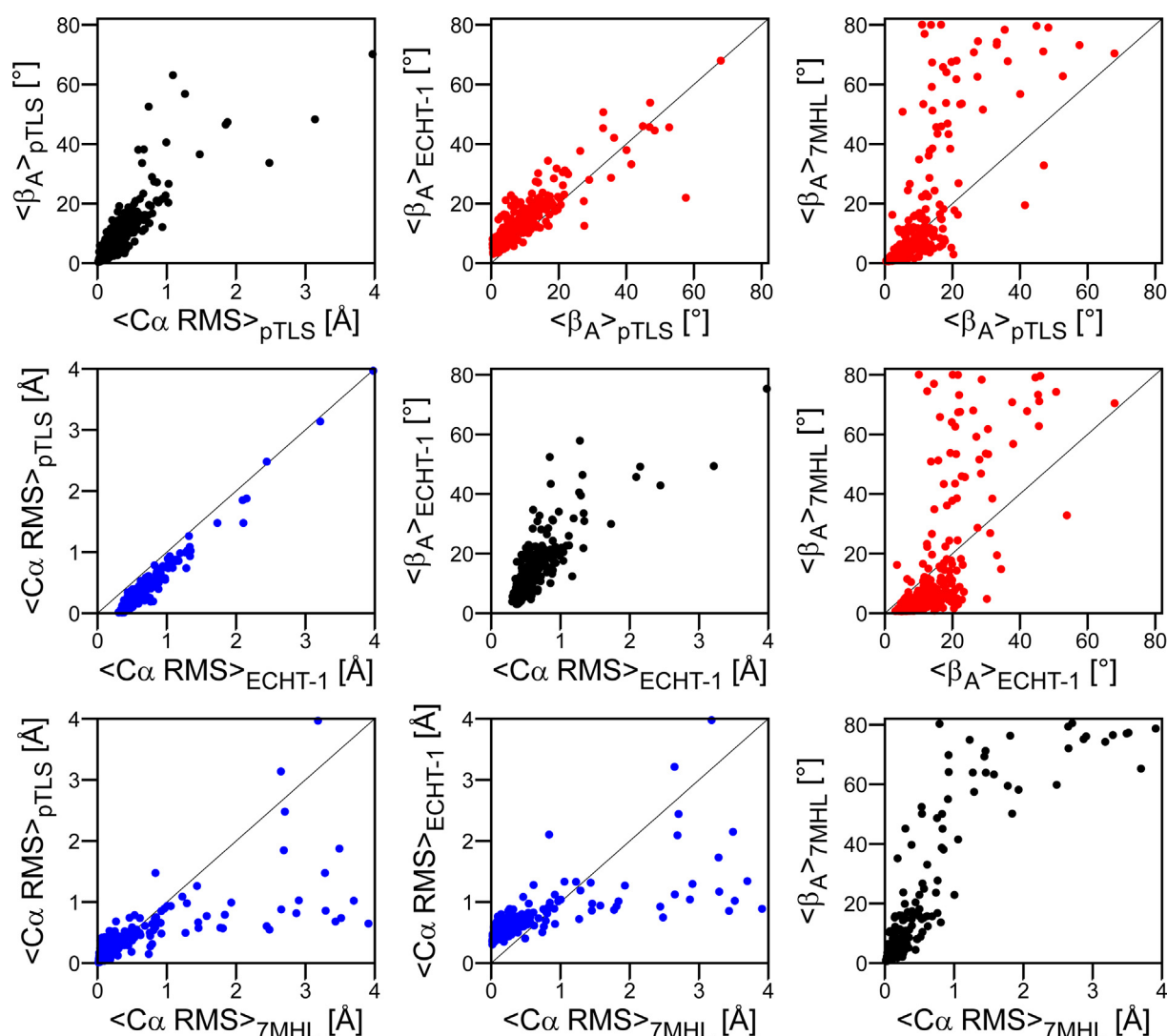
Figure 5. Comparisons of the rms spread in angular β_A excursions and C^α coordinate rmsd, with each point corresponding to a peptide plane for which RDCs were available. Diagonal panels show the correlations between rms β_A excursions and C^α coordinate rmsd (black). The left bottom three panels (blue) compare C^α coordinate rmsd for residues in the 7K3T pTLS and ECHT-1 ensembles with those of the 7MHL ensemble. The top right three panels (red) show correlations between β_A excursions of residues in these three ensembles.

ture.[53] In contrast to the 7K3T X-ray structure, the ensemble representations of the temperature series of X-ray structures showed no substantial improvement over their conventional multi-conformer representations (Table 2). This result is perhaps not surprising when considering that the angular dynamic excursions seen in the temperature series of the ensembles correlate poorly with one another (Figure S3). Indeed, even though the locations where increased dynamics is seen in terms of C^α rmsd are similar among the different ensembles (Figure 4a of Ebrahim *et al.*[31]), details of their backbone angular excursions are quite different. However, when merging the six ensemble representations of the temperature-dependent series into a single 281-member super-ensemble, the agreement with RDCs improved substantially and even exceeded that obtained for the 7K3T ensem-

ble. Merging the two 7K3T ensembles (pTLS and ECHT-1) with the 281-member super-ensemble resulted in a further ~7% improvement in Q_{jk} for this 381-member ensemble of ensembles, M$_{EE}^{pro}$ (Table 2, bottom row).

Interestingly, when comparing the RDC agreement for the least (L50%) and highest (H50%) dynamic residues in the individual ensembles recorded at different temperatures, the H50% halves of residues yielded much higher Q_{jk} factors than the least dynamic residues, by as much as 50% (Table 3). However, when considering the L and H halves of the M$_{EE}^{pro}$ super-ensemble, both halves fitted the RDCs remarkably well, with the M$_{EE}^{pro}$-H50% subset fitting even better than ($N = 2$) 7MHJ-L50%. However, the nearly 12% higher fitted D_a value for the H50% compared to the L50% fraction of residues indicates that the

Table 3 Fits of RDCs to X-ray structures for residues with the least (L50%) and most (H50%) disordered N—H and C′—H vectors in their X-ray ensemble representations.

Structure	T (K)	Resol. (Å)	R_{free}	N [a]	L50% [b] $<D_a>$	$Q_{jk}(^1D_{HN})$	$Q_{jk}(^2D_{C'H})$	H50% [b] $<D_a>$	$Q_{jk}(^1D_{HN})$	$Q_{jk}(^2D_{C'H})$	$\Gamma_{L50/H50}$ [c]
7K3T	100	1.2	0.187	2	12.794	0.210	0.226	12.642	0.324	0.324	1.012
7K3T-REDO	100	1.2	0.173	2	12.776	0.212	0.224	12.680	0.321	0.306	1.008
pTLS	100	1.2	0.169	50	12.991	0.194	0.208	13.556	0.274	0.267	0.958
ECHT-1	100	1.2	0.176	50	13.168	0.201	0.213	14.309	0.257	0.245	0.920
7MHF	100	1.55	0.224	2	12.779	0.233	0.209	12.505	0.306	0.303	1.022
7MHL	100	1.55	0.227	75	12.830	0.226	0.205	14.123	0.326	0.301	0.908
7MHG	240	1.53	0.205	2	12.872	0.252	0.222	12.370	0.251	0.257	1.041
7MHM	240	1.53	0.197	28	12.910	0.250	0.221	13.746	0.246	0.240	0.939
7MHH	277	2.19	0.253	2	13.042	0.236	0.232	11.967	0.367	0.350	1.090
7MHN	277	2.19	0.215	45	13.202	0.214	0.232	14.084	0.341	0.290	0.937
7MHI	298	1.88	0.228	2	13.135	0.188	0.211	11.991	0.291	0.295	1.095
7MHO	298	1.88	0.208	43	13.248	0.192	0.208	14.192	0.335	0.310	0.933
7MHJ	298 [d]	2.0	0.240	2	13.014	0.228	0.230	12.041	0.316	0.340	1.081
7MHP	298 [d]	2.0	0.221	54	13.139	0.214	0.215	14.528	0.305	0.244	0.904
7MHK	310	1.96	0.247	2	12.818	0.218	0.243	12.254	0.280	0.343	1.046
7MHQ	310	1.96	0.235	36	12.968	0.213	0.235	14.765	0.276	0.278	0.878
AF2-1 [e]				1	12.647	0.196	0.223	12.514	0.272	0.252	1.011
AF2-* [f]				25	12.662	0.195	0.222	12.591	0.271	0.250	1.005
7K3T+ [g]				100	13.136	0.201	0.206	13.910	0.256	0.248	0.944
7MH* [h]				281	13.133	0.192	0.199	14.912	0.246	0.212	0.881
MproEE [i]				381	13.209	0.188	0.195	14.773	0.224	0.203	0.894
MproEE + AF2 [j]				406	13.200	0.187	0.194	14.724	0.219	0.201	0.896
Xray* [k]				350	13.034	0.201	0.191	13.145	0.227	0.216	0.992
Xray*-VWfit [l]				350	12.725	0.195	0.189	12.843	0.218	0.206	0.991

[a] N is the number of conformers. X-ray structures and RDCs used are the same as for Table 2.

[b] L50% and H50% refer to the 50% fractions of residues that have the least and most disordered H-N and C′—H vectors in their ensemble representation. For the 7K3T and 7K3T-REDO structures, the angular RMSDs are taken from the ECHT-1 ensemble. For the top-scoring AlphaFold-multimer model, AF2-1, the angular RMSDs are from the 25-member AF2-* ensemble.

[c] $\Gamma_{L50/H50}$ is the ratio of D_a values for the L50% and H50% fraction of residues.

[d] At 99.5% relative humidity.

[e] Top AlphaFold2-multimer model.

[f] Unweighted combination of top 25 AlphaFold2-multimer models.

[g] Unweighted combined 7K3T pTLS and ECHT-1 ensembles.

[h] Unweighted combination of six ensembles of 7MHL-7MHQ, recorded at temperatures ranging from 100 to 308 K.

[i] Unweighted combination of all eight ensembles, incl. 7K3T pTLS and ECHT-1, and 7MHL-7MHQ.

[j] Unweighted combination of eight ensembles (MproEE) and the top 25 AlphaFold2-multimer models.

[k] Unweighted ensemble containing 350 static X-ray structures deposited in PDB (see Table S2).

[l] Weighted ensemble of 350 static X-ray structures with weights optimized by VWFit.[30]

amplitude of ensemble disorder for the H50% fraction of residues is considerably larger than their true disorder.

RDC fits to AlphaFold-Multimer models

The recently introduced AlphaFold protein structure prediction program, based on a deep neural network architecture, has proven particularly powerful at generating low energy structural models that agree exceptionally well with experimental structures.[54,55] AlphaFold and its successor AlphaFold2 can generate high quality models *de novo*, i.e. without access to previously solved structures that have significant sequence homology. However, with the availability of templates of previously solved homologous X-ray structures, AlphaFold2 was shown to generate models that agree even slightly better with NMR data than

the best experimental X-ray structures.[56] For M^pro, AlphaFold2 generated highly accurate models for the monomeric subunit, but with some uncertainty in the predicted models near the N-terminus and the active site, both involving significant inter-subunit interactions in the functional homodimeric state.[26] Recently introduced updates to the Alpha-Fold2 program now also enable the accurate prediction of protein complexes and we therefore used the AlphaFold2.2-Multimer (AF2-M) program[57] to generate M^pro homodimer models.

With combined predicted template modeling plus predicted interface template modeling (ptm + iptm) scores greater than 94% across the entire protein backbone, all of the top 25 AF2-M homodimer models showed high confidence and remarkably little variation among these models. Indeed, AlphaFold was designed to predict the lowest energy structure and the absence of significant
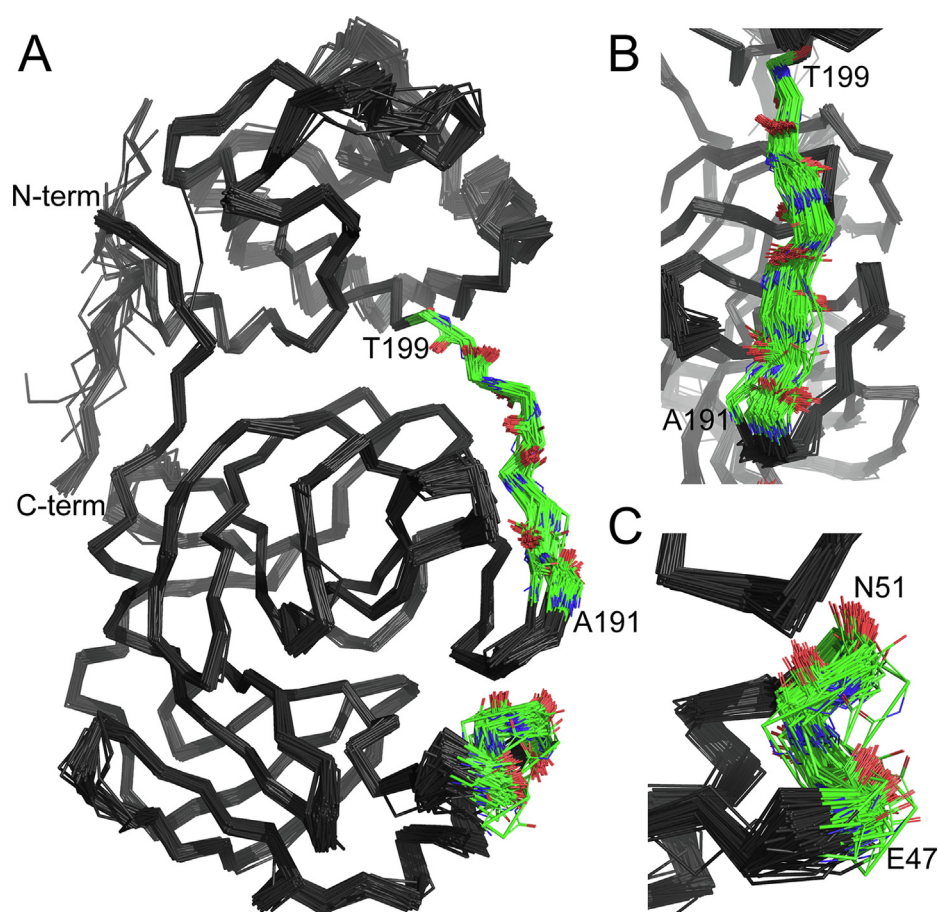
Figure 6. Backbone superposition of the 148 out of 350 M^{pro} X-ray structures that have above-average population in an ensemble that has been optimized to yield best agreement with RDCs. (A) Only the monomeric subunit of the active homodimeric M^{pro} enzyme is shown, with the N- and C-termini marked, and the high degree of disorder in the P2 helix and P5 loop shown in color. (B, C) Rotated views of the dynamic P2 and P5 substrate binding regions.

backbone disorder in the ensemble of accurately predicted structures is therefore not surprising (SI Table S4).

The presence of backbone dynamics also can be predicted on the basis of contacts between the backbone O and H^N atoms with heavy atoms of residues other than those forming the peptide bond.[58] Whereas this method predicts the presence of similar backbone dynamics for each of the top 25 AF2-M models (SI Table S4), roughly at the same positions as seen in the X-ray ensembles (Figure 4), there is no motional model associated with it. In contrast to the types of motions suggested by X-ray ensemble models, such an analysis therefore does not offer direct insights into the types of dynamic excursions.

RDC fits to an ensemble of conventional X-ray structures

There are 350 M^{pro} X-ray structures in the PDB that have coordinates for all residues and that have been recorded under a wide range of temperatures, ligation states, and crystallization

conditions, resulting in eight different space groups (Table S3). With $Q_{jk} = 0.26$, the 7K3T structure and its PDB-REDO equivalent rank among the best in a range that spans from $Q_{jk} = 0.26$–0.65 for this set of structures. When treating this collection of X-ray structures as an ensemble, the question arises whether any combination of these structures can yield an improved fit to the RDC data. Weight optimization of the individual ensemble members can be carried out with the previously introduced variable-weight fit program, VWfit,[30] but is time-consuming because of the iterative nature of the search and the large matrix sizes involved in the SVD fitting steps. Moreover, assigning weights to each of the 350 structures adds 349 adjustable parameters to the fit, and to avoid the effect of these additional degrees of freedom on the fit, it is important to carry out the weight optimization in a cross-validated manner. However, full jack-knife cross-validation requires the entire process to be repeated N times where N is the number of RDCs used in the fit, each time omitting a different RDC. To expedite the process, the VWfit search was modified to use a simu-

lated annealing approach for optimizing the weights, and the cross-validation was carried out by separating the RDCs into 10 randomly selected equal size non-overlapping fractions. Then, 9 fractions were used to optimize weights, and RDC agreement was evaluated for the fraction not used in the optimization, with the entire optimization repeated 10 times.

While most of these X-ray structures were determined by molecular replacement procedures, the orientational distribution of backbone bond vectors of the 350-member ensemble is fairly heterogeneous (Figure 3). However, when using Eq. (3) to express these distributions in terms of generalized order parameters, S, the degree of disorder is considerably smaller than seen for the two ensemble refinements of 7K3T (Figure 4(A)) and for the temperature series of ensembles (Figure 4(B)).

Starting from an equally weighted distribution, VWfit converged to a reasonably well-defined set of weights, w_i, not dominated by individual ensemble members (SI Figure S6). Backbone superposition of the 148 X-ray structures that had above average weights shows considerable structural heterogeneity, in particular for the P2 helix and the P5 loop (Figure 6).

Remarkably, the ensemble with optimized weights provides an even slightly better fit to the RDCs than any combination derived above from the dynamic ensembles (Table 2). Importantly, when separately considering the RDC fits to the most disordered H50% fraction of this ensemble, the fitted D_a value is nearly the same as that for the least disordered half, L50% (Table 3). This result indicates that the degree of disorder reflected in this ensemble of conventionally refined X-ray structures, which is quite large in some regions of the protein (Figure 6), is in good quantitative agreement with RDCs.

Concluding remarks

Our prior analysis of M^{pro} RDCs showed good agreement with conventionally refined high-resolution crystal structures for two contiguous stretches of residues in the N- and C-terminal domains,[26] while attributing the poorer fit for the remaining regions to internal dynamics as well as several real differences in structure between the solution and crystalline states of the protein. An example of the latter concerns the amide group of Thr-198, at the C-terminal end of the P5 substrate binding pocket. This residue constitutes the largest outlier in the SVD fit to 7K3T and its ensemble representations, but its RDCs fit very well to the 1.75-Å 6Y2E crystal structure of Zhang *et al.*[59] The RDCs of Thr-198 also fit well to both the conventional and ensemble representations of X-ray structures collected at 277 and 298 K, but not to those recorded at 100, 240 and 310 K (SI Figure S5),

pointing to true differences in the diffraction data despite all being in the same space group (C_{121}).

The lower fitted D_a value for the pTLS 7K3T compared to the ECHT-1 ensemble (Table 2) reflects less disorder in their bond vector orientations, without indicating which representation is more realistic. However, when comparing the fitted D_a values obtained for the most disordered H50% and least disordered L50% residues of the ensembles, a nearly 10% increase in the fitted D_a values is observed for the more dynamic half. The differences are even larger for the temperature series of X-ray structures (Table 3). For a quantitatively correct representation of the dynamics in an ensemble, the fitted D_a values should be the same for the L50% and H50% fractions of residues. As expected, for the conventionally refined X-ray structures the opposite behavior is seen, with the fitted D_a values for H50% being smaller than for L50%. This result indicates that residues identified in the ensemble as "dynamic" (H50%) have RDCs that are only moderately reduced in magnitude by motional averaging, by much less than indicated by the ensemble presentation (*cf* Eq. (3)). So, while the X-ray ensembles correctly identify the more dynamic residues, the differences in the amplitudes of the dynamics assigned to the H50% and L50% groups of residues are considerably too large, in particular for the temperature series of ensembles (7MHL-7MHQ). This overly dynamic behavior of the least ordered residues must result from the MD force field together with the weight given to fitting the electron densities during the restrained MD calculation. It is plausible that ensembles generated by the newer ECHT ensemble refinement technology, including DEN restraints, can improve the RDC fits for this temperature series of X-ray data over the results available in the PDB. However, we note that the intrinsic resolution of these data sets is lower than for the 1.2-Å 7K3T data, and optimization of the protocol will require adjustment of the weight of DEN restraints, relaxation time (TX) and X-ray weight (XW) parameters, requiring vast amounts of compute time.

Remarkably, when considering all 350 M^{pro} X-ray structures in the PDB that lack gaps in their sequence as a representation of a dynamic ensemble, far better agreement with RDC data is obtained than for any individual structure. In fact, this pseudo-ensemble also fits somewhat better than the best ensemble refinement obtained for the highest resolution X-ray structure (Table 2), even though many of the individual X-ray structures fit the RDC data rather poorly. Importantly, the observation that RDC-fits to the most ordered (H50%) and least ordered (L50%) residues yield the same D_a values indicates that the amplitude and direction of conformational differences seen between these X-ray structures

are quantitatively consistent with the conformational distribution sampled by the protein in solution on the time scale of pico- to milliseconds.

Our analysis of the 1.2-Å X-ray structure of M^{pro} showed an improvement in RDC fit by more than 10% when comparing the fit of the pTLS ensemble coordinates with that of the *PDB-REDO* conventionally re-refined model (Table 2), and a further improvement by *ca* 2% for the ECHT-1 ensemble. Perhaps surprisingly, another *ca* 10% improvement in RDC agreement was obtained when combining these two ensembles with the six ensembles reported by Ebrahim *et al.*[31] for lesser resolution crystal structures recorded at different temperatures. While all these ensembles qualitatively agree on the location of more dynamic sites, the fact that their joint evaluation improves the fit to the solution RDCs indicates that none of these individual ensembles provides a perfect quantitative description of the internal protein dynamics. We note that the number of conformers used in the X-ray ensembles is not a limiting factor because dipolar couplings have a smooth, rank-2 tensorial dependence on orientation (Eq. (1)) and a modest number of conformers therefore can suffice to describe their distribution. Instead, the rather large quantitative differences in angular distributions seen in the different ensembles (Figures 3 and 5; Figure S3) suggest that the X-ray data provided insufficient restraining power to quantitatively assign residue-specific motions for each backbone amide moiety. Our finding that the combined use of eight ensembles resulted in improved agreement with solution RDCs also suggests that further improvements to X-ray ensemble refinement may be feasible, and that these potentially could benefit from adding RDC restraints to the MD protocol that currently only uses electron density as experimental restraints.

Methods

Validation of structural models by RDCs

For protein X-ray crystallography, the agreement between structure factors and a derived model is represented by the *R* factor, but because these structure factors are used to adjust atomic coordinates for optimizing this agreement *R* is not a true indicator of structural accuracy. Instead, cross validation has been introduced where the structure is calculated using only a large fraction of the Bragg reflections, and consistency of the model is evaluated by agreement with reflections not used in model generation,[10] represented by the R_{free} factor. Its value complements R_{work}, which reports on the agreement with the data used for refinement.

Similar considerations apply to an even greater extent for NMR structures determined with inclusion of RDC restraints, which can result in near-perfect RDC agreement with the atomic coordinates even if models are wrong.[60] A quality factor, *Q*, is often used that is defined by

$$Q = \sqrt{\sum_{i=1..N}(D_i^{pred} - D_i^{meas})^2 / [N\{D_a^2(4+3Rh^2)/5\}]} \qquad (5)$$

where D^{pred} and D^{meas} refer to the best-fitted and experimental RDCs, respectively, with D_a and *Rh* being the alignment strength and rhombicity obtained from the SVD fit. The denominator represents the predicted root-mean-square value of a large set of vectors randomly distributed in orientation for an alignment strength defined by D_a and *Rh*.[44]

Jackknifed Q factors for agreement between RDCs and coordinates

Analogous to X-ray crystallography, a cross-validated Q_{free} factor can be used to evaluate the quality of NMR structures that include RDCs as input restraints. For this purpose, the structure calculation is repeated *N* times, each time omitting a different 1/N fraction of the RDCs that are then used for deriving Q_{free}.[44]

Even when evaluating structures that were derived without RDCs as input restraints, there is a small tendency to overestimate the agreement between RDCs and coordinates because five adjustable parameters are used in the SVD fit. When the number of RDCs used in the fit is not very much larger than this number of fitted parameters, the correlation between observed RDCs and those predicted for the structure exceeds its true value. To remove this bias, for fitting a set of *N* RDCs in this study we use a standard jackknife procedure where the SVD is repeated *N* times, each time leaving out a single, different RDC. For each measured RDC, its predicted value is then derived by using all *N*-1 remaining RDCs to determine the alignment tensor as well as the predicted value of the left-out RDC. This procedure makes *Q* effectively independent of the number of RDCs used in the fit. To distinguish this jackknifed *Q* factor from its more widely used implementation that uses a single SVD fit to calculate predicted RDCs, we refer to it as Q_{jk}.

$$Q_{jk} = \sqrt{\sum_{q=1..N} \frac{(D_q^{pred} - D_q^{meas})^2}{N\{D_{a,q}^2(4+3Rh_q^2)/5\}}} \qquad (6)$$

where D_q^{meas} and D_q^{pred} refer to the measured RDC and the predicted RDC when the SVD is carried out for all residues except *q*, and $D_{a,q}$ and Rh_q are the D_a and *Rh* values obtained for these SVD fits. The use of Q_{jk} rather than *Q* becomes important when comparing fits of small numbers of RDCs to their corresponding atomic coordinates, or when judging the merits of different structures having nearly the same *Q* values.

AlphaFold2-Multimer model generation

AlphaFold2-Multimer source code (version 2.2.0) was downloaded from the GitHub repository (https://github.com/deepmind/alphafold), with the requisite databases retrieved by using the included script. AlphaFold2-Multimer was run, unmodified, with a date limit of 01–01-3000 (full) and otherwise default parameters. For each AlphaFold2-Multimer calculation, a total of 25 models were obtained while the five models with the highest average per-residue predicted local-distance difference test (iptm + ptm) confidence score were retained for further analysis. The calculation was repeated five times with different random seeds to generate a 25-member ensemble of top-5 models that was used for further analysis.

CRediT authorship contribution statement

Yang Shen: Investigation, Writing – original draft, Writing – review & editing. **Angus J. Robertson:** Writing – review & editing. **Ad Bax:** Conceptualization, Supervision, Writing – review & editing.

Declaration of Competing Interest

The authors declare that they have no known competing financial interests or personal relationships that could have appeared to influence the work reported in this paper.

Appendix A. Supplementary material

Supplementary material to this article can be found online at https://doi.org/10.1016/j.jmb.2023.168067.

† Current address: Biophysical Chemistry, Center for Molecular Protein Science, Lund University, 22100 Lund, Sweden.

References

1. Frauenfelder, H., Petsko, G.A., Tsernoglou, D., (1979). Temperature-dependent X-ray diffraction as a probe of protein structural dynamics. *Nature* **280**, 558–563.
2. van den Bedem, H., Dhanik, A., Latombe, J.C., Deacon, A. M., (2009). Modeling discrete heterogeneity in X-ray diffraction data by fitting multi-conformers. *Acta Crystallogr. Sect. D-Struct. Biol.* **65**, 1107–1117.
3. Davis, I.W., Arendall, W.B., Richardson, D.C., Richardson, J.S., (2006). The backrub motion: How protein backbone shrugs when a sidechain dances. *Structure* **14**, 265–274.
4. Powers, R., Clore, G.M., Garrett, D.S., Gronenborn, A.M., (1993). Relationships between the precision of high-resolution protein NMR structures, solution-order parameters, and crystallographic B factors. *J. Magn. Reson. B* **101**, 325–327.
5. Fenwick, R.B., van den Bedem, H., Fraser, J.S., Wright, P. E., (2014). Integrated description of protein dynamics from room-temperature X-ray crystallography and NMR. *Proc. Natl. Acad. Sci. USA* **111**, E445–E454.
6. Adams, P.D., Grosse-Kunstleve, R.W., Hung, L.W., Ioerger, T.R., McCoy, A.J., Moriarty, N.W., Read, R.J., Sacchettini, J.C., et al., (2002). PHENIX: building new software for automated crystallographic structure determination. *Acta Crystallogr. Sect. D-Struct. Biol.* **58**, 1948–1954.
7. Adams, P.D., Afonine, P.V., Bunkoczi, G., Chen, V.B., Davis, I.W., Echols, N., Headd, J.J., Hung, L.W., et al., (2010). PHENIX: a comprehensive Python-based system for macromolecular structure solution. *Acta Crystallogr. Sect. D-Struct. Biol.* **66**, 213–221.
8. Gros, P., Vangunsteren, W.F., Hol, W.G.J., (1990). Inclusion of thermal motion in crystallographic structures by restrained molecular dynamics. *Science* **249**, 1149–1152.
9. Torda, A.E., Scheek, R.M., van Gunsteren, W.F., (1989). Time-dependent distance restraints in molecular dynamics simulations. *Chem. Phys. Lett.* **157**, 289–294.
10. Brunger, A.T., (1992). Free R-value – a novel statistical quantity for assessing the accuracy of crystal-structures. *Nature* **355**, 472–475.
11. Burling, F.T., Brunger, A.T., (1994). Thermal motion and conformational disorder in protein crystal structures – Comparison of multi-conformer and time-averaging models. *Isr. J. Chem.* **34**, 165–175.
12. Clarage, J.B., Phillips, G.N., (1994). Cross-validation tests of time-averaged molecular dynamics refinements for determinatin of protein structures by X-ray crystallography. *Acta Crystallogr. Sect. D-Biol. Crystallogr.* **50**, 24–36.
13. Burnley, B.T., Afonine, P.V., Adams, P.D., Gros, P., (2012). Modelling dynamics in protein crystal structures by ensemble refinement. *Elife* **1**, e00311.
14. Zou, H., Hastie, T., (2005). Regularization and variable selection via the elastic net. *J. R. Stat. Soc. Ser. B-Stat. Methodol.* **67**, 301–320.
15. Pearce, N.M., Gros, P., (2021). A method for intuitively extracting macromolecular dynamics from structural disorder. *Nature Commun.* **12**, 5493.

16. Schroder, G.F., Levitt, M., Brunger, A.T., (2014). Deformable elastic network refinement for low-resolution macromolecular crystallography. *Acta Crystallogr. Sect. D-Struct. Biol.* **70**, 2241–2255.

17. Winn, M.D., Isupov, M.N., Murshudov, G.N., (2001). Use of TLS parameters to model anisotropic displacements in macromolecular refinement. *Acta Crystallogr. Sect. D-Struct. Biol.* **57**, 122–133.

18. Urzhumtsev, A., Afonine, P.V., Van Benschoten, A.H., Fraser, J.S., Adams, P.D., (2015). From deep TLS validation to ensembles of atomic models built from elemental motions. *Acta Crystallogr. Sect. D-Struct. Biol.* **71**, 1668–1683.

19. Meisburger, S.P., Case, D.A., Ando, N., (2020). Diffuse X-ray scattering from correlated motions in a protein crystal. *Nature Commun.* **11**, 1271.

20. Andi, B., Kumaran, D., Kreitler, D.F., Soares, A.S., Keereetaweep, J., Jakoncic, J., Lazo, E.O., Shi, W.X., et al., (2022). Hepatitis C virus NS3/4A inhibitors and other drug-like compounds as covalent binders of SARS-CoV-2 main protease. *Sci. Rep.* **12**, 12197.

21. Joosten, R.P., Salzemann, J., Bloch, V., Stockinger, H., Berglund, A.-C., Blanchet, C., Bongcam-Rudloff, E., Combet, C., et al., (2009). PDB_REDO: automated re-refinement of X-ray structure models in the PDB. *J. Appl. Cryst.* **42**, 376–384.

22. Chiliveri, S.C., Robertson, A.J., Shen, Y., Torchia, D.A., Bax, A., (2022). Advances in NMR Spectroscopy of Weakly Aligned Biomolecular Systems. *Chem. Rev.* **122**, 9307–9330.

23. Prestegard, J.H., Al-Hashimi, H.M., Tolman, J.R., (2000). NMR structures of biomolecules using field oriented media and residual dipolar couplings. *Q. Rev. Biophys.* **33**, 371–424.

24. Tolman, J.R., Al-Hashimi, H.M., Kay, L.E., Prestegard, J.H., (2001). Structural and Dynamic Analysis of Residual Dipolar Coupling Data for Proteins. *J. Am. Chem. Soc.* **123**, 1416–1424.

25. Peti, W., Meiler, J., Bruschweiler, R., Griesinger, C., (2002). Model-free analysis of protein backbone motion from residual dipolar couplings. *J. Am. Chem. Soc.* **124**, 5822–5833.

26. Robertson, A.J., Courtney, J.M., Shen, Y., Ying, J.F., Bax, A., (2021). Concordance of X-ray and AlphaFold2 Models of SARS-CoV-2 Main Protease with Residual Dipolar Couplings Measured in Solution. *J. Am. Chem. Soc.* **143**, 19306–19310.

27. Tolman, J.R., Flanagan, J.M., Kennedy, M.A., Prestegard, J.H., (1997). NMR evidence for slow collective motions in cyanometmyoglobin. *Nature Struct. Biol.* **4**, 292–297.

28. Salmon, L., Bouvignies, G., Markwick, P., Lakomek, N., Showalter, S., Li, D.W., Walter, K., Griesinger, C., et al., (2009). Protein Conformational Flexibility from Structure-Free Analysis of NMR Dipolar Couplings: Quantitative and Absolute Determination of Backbone Motion in Ubiquitin. *Angew. Chem. Int. Ed.* **48**, 4154–4157.

29. Chen, K., Tjandra, N., (2012). The Use of Residual Dipolar Coupling in Studying Proteins by NMR. In: Zhu, G. (Ed.)*, NMR of Proteins and Small Biomolecules*, pp. 47–67.

30. Maltsev, A.S., Grishaev, A., Roche, J., Zasloff, M., Bax, A., (2014). Improved cross validation of a static ubiquitin structure derived from high precision residual dipolar couplings measured in a drug-based liquid crystalline phase. *J. Am. Chem. Soc.* **136**, 3752–3755.

31. Ebrahim, A., Riley, B.T., Kumaran, D., Andi, B., Fuchs, M.R., McSweeney, S., Keedy, D.A., (2022). The temperature-dependent conformational ensemble of SARS-CoV-2 main protease (M-pro). *Iucrj* **9**, 682–694.

32. Ploscariu, N., Burnley, T., Gros, P., Pearce, N.M., (2021). Improving sampling of crystallographic disorder in ensemble refinement. *Acta Crystallogr. Sect. D-Struct. Biol.* **77**, 1357–1364.

33. Losonczi, J.A., Andrec, M., Fischer, M.W.F., Prestegard, J.H., (1999). Order matrix analysis of residual dipolar couplings using singular value decomposition. *J. Magn. Reson.* **138**, 334–342.

34. Bax, A., Kontaxis, G., Tjandra, N., (2001). Dipolar couplings in macromolecular structure determination. *Meth. Enzymol.* **339**, 127–174.

35. Hansen, M.R., Mueller, L., Pardi, A., (1998). Tunable alignment of macromolecules by filamentous phage yields dipolar coupling interactions. *Nature Struct. Biol.* **5**, 1065–1074.

36. Ulmer, T.S., Ramirez, B.E., Delaglio, F., Bax, A., (2003). Evaluation of backbone proton positions and dynamics in a small protein by liquid crystal NMR spectroscopy. *J. Am. Chem. Soc.* **125**, 9179–9191.

37. Schwieters, C.D., Kuszewski, J.J., Clore, G.M., (2006). Using Xplor-NIH for NMR molecular structure determination. *Prog. Nucl. Magn. Reson. Spectrosc.* **48**, 47–62.

38. Koradi, R., Billeter, M., Wuthrich, K., (1996). MOLMOL: a program for display and analysis of macromolecular structures. *J. Mol. Graph.* **14**, 51–55.

39. Das, R., Baker, D., (2008). Macromolecular modeling with Rosetta. *Annu. Rev. Biochem.* **77**, 363–382.

40. Delaglio, F., Grzesiek, S., Vuister, G.W., Zhu, G., Pfeifer, J., Bax, A., (1995). NMRPipe: a multidimensional spectral processing system based on UNIX pipes. *J. Biomol. NMR* **6**, 277–293.

41. Chen, V.B., Arendall III, W.B., Headd, J.J., Keedy, D.A., Immormino, R.M., Kapral, G.J., Murray, L.W., Richardson, J.S., et al., (2010). MolProbity: all-atom structure validation for macromolecular crystallography. *Acta Crystallogr. Sect. D-Biol. Crystallogr.* **66**, 12–21.

42. Ottiger, M., Bax, A., (1998). Determination of relative N-H-N N-C ', C-alpha-C ', andC(alpha)-H-alpha effective bond lengths in a protein by NMR in a dilute liquid crystalline phase. *J. Am. Chem. Soc.* **120**, 12334–12341.

43. Cornilescu, G., Marquardt, J.L., Ottiger, M., Bax, A., (1998). Validation of protein structure from anisotropic carbonyl chemical shifts in a dilute liquid crystalline phase. *J. Am. Chem. Soc.* **120**, 6836–6837.

44. Clore, G.M., Garrett, D.S., (1999). R-factor, free R, and complete cross-validation for dipolar coupling refinement of NMR structures. *J. Am. Chem. Soc.* **121**, 9008–9012.

45. Fitzkee, N.C., Bax, A., (2010). Facile measurement of H-1-N-15 residual dipolar couplings in larger perdeuterated proteins. *J. Biomol. NMR* **48**, 65–70.

46. Bax, A., (2003). Weak alignment offers new NMR opportunities to study protein structure and dynamics. *Protein Sci.* **12**, 1–16.

47. Lipari, G., Szabo, A., (1982). Model-free approach to the interpretation of nuclear magnetic resonance relaxation in macromolecules. 1. Theory and range of validity. *J. Am. Chem. Soc.* **104**, 4546–4559.

48. Fadel, A.R., Jin, D.Q., Montelione, G.T., Levy, R.M., (1995). Crankshaft Motions of the Polypeptide Backbone

in Molecular-Dynamics Simulations of Human Type-Alpha Transforming Growth-Factor. *J. Biomol. NMR* **6**, 221–226.

49. Lienin, S.F., Bremi, T., Brutscher, B., Bruschweiler, R., Ernst, R.R., (1998). Anisotropic intramolecular backbone dynamics of ubiquitin characterized by NMR relaxation and MD computer simulation. *J. Am. Chem. Soc.* **120**, 9870–9879.

50. Lange, O.F., Lakomek, N.A., Fares, C., Schroder, G.F., Walter, K.F.A., Becker, S., Meiler, J., Grubmuller, H., et al., (2008). Recognition dynamics up to microseconds revealed from an RDC-derived ubiquitin ensemble in solution. *Science* **320**, 1471–1475.

51. Yao, L., Vogeli, B., Torchia, D.A., Bax, A., (2008). Simultaneous NMR study of protein structure and dynamics using conservative mutagenesis. *J. Phys. Chem. B* **112**, 6045–6056.

52. Meier, S., Haussinger, D., Jensen, P., Rogowski, M., Grzesiek, S., (2003). High-accuracy residual H-1(N)-C-13 and H-1(N)-H-1(N) dipolar couplings in perdeuterated proteins. *J. Am. Chem. Soc.* **125**, 44–45.

53. Fraser, J.S., van den Bedem, H., Samelson, A.J., Lang, P. T., Holton, J.M., Echols, N., Alber, T., (2011). Accessing protein conformational ensembles using room-temperature X-ray crystallography. *Proc. Natl. Acad. Sci. U. S. A.* **108**, 16247–16252.

54. Jumper, J., Evans, R., Pritzel, A., Green, T., Figurnov, M., Ronneberger, O., Tunyasuvunakool, K., Bates, R., et al., (2021). Highly accurate protein structure prediction with AlphaFold. *Nature* **596**, 583–589.

55. Kryshtafovych, A., Schwede, T., Topf, M., Fidelis, K., Moult, J., (2021). Critical assessment of methods of protein structure prediction (CASP)-Round XIV. *Proteins-Struct. Funct. Bioinform.* **89**, 1607–1617.

56. Zweckstetter, M., (2021). NMR hawk-eyed view of AlphaFold2 structures. *Protein Sci.* **30**, 2333–2337.

57. Evans, R., O'Neill, M., Pritzel, A., Antropova, N., Senior, A., Green, T., Žídek, A., Bates, R., et al., 2021. Protein complex prediction with AlphaFold-Multimer.

58. Zhang, F.L., Brüschweiler, R., (2002). Contact model for the prediction of NMR N-H order parameters in globular proteins. *J. Am. Chem. Soc.* **124**, 12654–12655.

59. Zhang, L., Lin, D., Sun, X., Curth, U., Drosten, C., Sauerhering, L., Becker, S., Rox, K., et al., (2020). Crystal structure of SARS-CoV-2 main protease provides a basis for design of improved α-ketoamide inhibitors. *Science* **368**, 409–412.

60. Bax, A., Grishaev, A., (2005). Weak alignment NMR: a hawk-eyed view of biomolecular structure. *Curr. Opin. Struct. Biol.* **15**, 563–570.